Observed crustal uplift near the Southern Patagonian Icefield constrains improved viscoelastic Earth models

H. Lange[1], G. Casassa[2,3], E. R. Ivins[4], L. Schröder[1], M. Fritsche[1], A. Richter[1,5], A. Groh[1], and R. Dietrich[1]

[1]Institut für Planetare Geodäsie, Technische Universität Dresden, Dresden, Germany, [2]Formerly at Centro de Estudios Científicos, Valdivia, Chile, [3]Now at Geoestudios, Santiago, Chile and Universidad de Magallanes, Punta Arenas, Chile, [4]Jet Propulsion Laboratory, California Institute of Technology, Pasadena, California, USA, [5]Facultad de Ciencias Astronómicas y Geofísicas, Universidad Nacional de La Plata, La Plata, Argentina

Abstract Thirty-one GPS geodetic measurements of crustal uplift in southernmost South America determined extraordinarily high trend rates (> 35 mm/yr) in the north-central part of the Southern Patagonian Icefield. These trends have a coherent pattern, motivating a refined viscoelastic glacial isostatic adjustment model to explain the observations. Two end-member models provide good fits: both require a lithospheric thickness of 36.5 ± 5.3 km. However, one end-member has a mantle viscosity near $\eta = 1.6 \times 10^{18}$ Pa s and an ice collapse rate from the Little Ice Age (LIA) maximum comparable to a lowest recent estimate of 1995–2012 ice loss at about −11 Gt/yr. In contrast, the other end-member has much larger viscosity: $\eta = 8.0 \times 10^{18}$ Pa s, half the post–LIA collapse rate, and a steadily rising loss rate in the twentieth century after AD 1943, reaching −25.9 Gt/yr during 1995–2012.

1. Introduction

The Southern Patagonian Icefield (Figure 1) represents the largest temperate ice mass within the Southern Hemisphere with an area of 12,500 km^2 in the year 2000 [*Casassa et al.*, 2014]. It experienced significant ice mass variations during the Pleistocene and Holocene and its present-day negative ice mass balance is substantial for its size. There has been an increasing rate of mass loss during the last 70 years [*Rignot et al.*, 2003], exceeding −20 Gt/yr during the period 2000–2012 [*Willis et al.*, 2012]. These changing ice loads cause a glacial isostatic adjustment (GIA) of the solid Earth. The tectonic setting of the region is one of the relatively young (< 12 Ma) ocean ridge subduction with concomitant slab-window formation and deeper mantle upwelling. Five such slab windows are currently active on the eastern Pacific Rim [*McCrory et al.*, 2009] and each is likely to have a comparatively thin lithospere and low-viscosity upper mantle. Low-viscosity mantle has been shown to exist in southern Alaska by *Larsen et al.* [2005] using GIA studies. In this paper we are able to probe the allowable viscosity range for the upper mantle within the Patagonian slab window. Determining this fundamental constitutive parameter might allow us, eventually, to better understand the dynamics of oceanic lithospheric subduction throughout the eastern edge of the Pacific Rim. The viscoelastic response of the solid Earth to ice mass changes above this slab-window mantle is, therefore, comparatively fast, and the observed vertical crustal movements can reach about 40 mm/yr [*Dietrich et al.*, 2010]. However, until now there have not been sufficient observations to well-constrain the parameters that exist in a host of possible GIA models [*Ivins and James*, 1999, 2004; *Klemann et al.*, 2007] over the whole area of the Southern Patagonian Icefield (SPI). This is of special importance if mass changes are recorded by Gravity Recovery and Climate Experiment (GRACE), since ice mass and solid Earth components need to be separated for determining the contribution of ice loss to global mean sea level rise [*Ivins et al.*, 2011; *Gardner et al.*, 2013]. In this paper we present new uplift rates observed by GPS around and within the bedrock environment of the SPI at total of 31 sites, spanning the SPI. The area coverage of the data, therefore, holds promise for constraining the effective lithospheric thickness over decadal to millennial timescales, a geophysical observation that has been elusive outside of the realm of postseismic related deformation observations [e. g., *Thatcher and Pollitz*, 2008; *Larsen et al.*, 2005]. The data set provides a sound basis for improving the GIA model, specifically its Earth model and the load model, for the lithosphere/mantle parameters and for evaluating the ice unloading history since the Little Ice Age (LIA) maximum in the mid-seventeenth century [*Glasser et al.*, 2011].
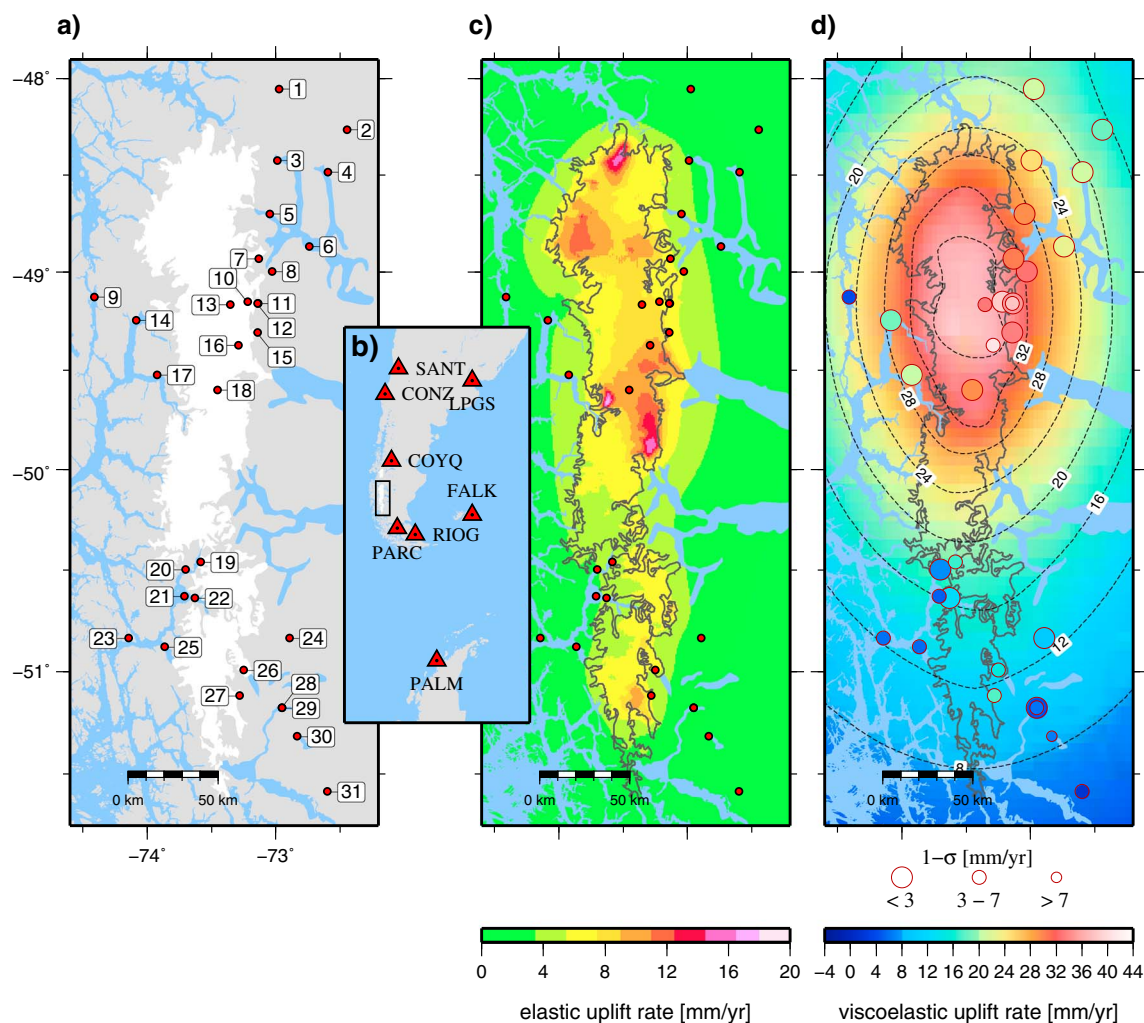
Figure 1. (a) Southern Patagonian Icefield with GPS stations. (b) International Global Navigation Satellite Systems (GNSS) Service (IGS) stations used in the data analysis. (c) Estimation of elastic uplift rates, based on present-day ice loss published by *Willis et al.* [2012]. Red dots indicate GPS sites of this study. (d) Comparison of refined viscoelastic Model A with observed uplift rates (color-coded disks).

2. Data Acquisition and Analysis

2.1. Site Locations, Equipment, and Observations

Precise GPS observations have been carried out in the area of the SPI since 1996. Figure 1a gives an overview of the distribution of 31 GPS sites which have been observed repeatedly. The extension of the network is about 380 km in north-south and 130 km in east-west direction. Every station was monumented by a firmly embedded, steel or brass bedrock marker. At 23 stations the geodetic GPS antennas were directly mounted on these markers. Only at three early sites it was necessary to use a tripod and on five remaining sites a tribrach was used for antenna setup. During the first expeditions to the SPI (1996, 2001) the stations (10), (12), (14), (15) (16), (18), and (28) were monumented and observed. In the year 2003, eight stations (1), (2), (3), (4), (5), (6), (8), and (11) were established in the area of Lago O'Higgins in the northern part of the SPI. Subsequent field campaigns permitted the incorporation of the locations (7), (9), (13), (17), and (20). Since 2009, expeditions expanded to the southern edge of the SPI yielding new monuments and repeated GNSS measurements of nine temporary stations (19), (21), (23), (25), (26), (27), (29), (30), and (31), near Fiordo Calvo and in the area of the Torres del Paine National Park. Additionally, continuous GNSS observations were collected at two permanent sites (22) and (24) for a time span of more than 2 years. During the early campaigns 1996–2001 TOPCON Turbo SII / AOA-RASCAL dual-frequency GPS receivers and antennas were employed. From 2003 to 2006 mainly Trimble 4000SSI receivers with Trimble compact and Trimble geodetic antennas were used. Since 2009, Trimble R7, Leica GRX1200+ geodetic GNSS-receivers and Trimble Zephyr

Table 1. Summary of Site Coordinates, Observation Periods, Antenna-Installation Type, and Vertical Uplift Results[a]

Station #	Lat (°)	Lon (°)	Height (m)	Year of 1st Occup.	Last Occup.	Total Camp.	# of Sess.	Inst.Type /Ant. Chg.	Uplift Rates (mm/yr) Observed	Elast.	Mod A	Mod B
1	−48.055	−72.973	268	2003	2010	4	31	D/-	21 ± 2	2	21	19
2	−48.265	−72.444	468	2003	2010	4	38	D/-	18 ± 3	2	18	17
3	−48.425	−72.990	347	2003	2010	3	23	D/-	25 ± 2	3	25	24
4	−48.485	−72.594	384	2003	2010	6	120	D/-	21 ± 2	2	21	20
5	−48.702	−73.046	332	2003	2010	3	24	D/-	30 ± 2	4	28	29
6	−48.868	−72.740	320	2003	2010	3	21	D/-	23 ± 2	3	26	25
7	−48.931	−73.134	303	2006	2010	2	15	D/-	30 ± 3	6	31	33
8	−48.997	−73.028	289	2003	2010	5	73	D/-	33 ± 2	5	30	31
9	−49.126	−74.409	56	2008	2011	2	5	D/A	4 ± 6	3	23	23
10	−49.151	−73.217	1593	1998	2010	3	4	T/A	39 ± 3	8	32	35
11	−49.159	−73.139	1631	2003	2010	5	40	D/-	35 ± 2	7	31	34
12	−49.160	−73.140	1608	1998	2010	3	8	T/A	38 ± 4	7	32	34
13	−49.166	−73.353	1721	2007	2010	2	8	D/A	33 ± 4	9	33	37
14	−49.246	−74.087	16	1996	2011	3	16	T/A	19 ± 2	3	28	29
15	−49.307	−73.142	1424	2001	2010	2	7	T/A	33 ± 3	7	31	35
16	−49.371	−73.290	1246	2001	2010	2	5	T/A	41 ± 3	10	33	38
17	−49.521	−73.921	85	2006	2011	2	12	T/-	20 ± 3	4	28	30
18	−49.599	−73.454	1593	1996	2010	3	10	T/A	30 ± 2	11	30	34
19	−50.459	−73.583	21	2009	2011	2	8	D/-	17 ± 5	4	15	19
20	−50.497	−73.701	105	2008	2011	4	16	D/A	7 ± 2	3	15	18
21	−50.629	−73.709	16	2009	2011	3	14	D/-	5 ± 5	3	13	16
22	−50.637	−73.628	31	2009	2011	cont.	732	D/-	13 ± 2	4	13	16
23	−50.835	−74.146	47	2009	2011	3	17	D/-	6 ± 4	2	9	12
24	−50.836	−72.894	283	2009	2012	cont.	864	D/-	10 ± 2	3	10	13
25	−50.878	−73.865	16	2009	2011	3	17	D/-	6 ± 7	3	10	13
26	−50.992	−73.248	184	2009	2011	2	22	D/-	15 ± 3	5	9	13
27	−51.119	−73.280	368	2009	2011	2	22	D/-	18 ± 3	6	8	11
28	−51.177	−72.953	45	1999	2009	2	7	T/A	4 ± 2	2	7	10
29	−51.178	−72.952	60	2009	2011	3	30	D/-	6 ± 6	2	7	10
30	−51.317	−72.834	63	2009	2011	3	28	D/-	7 ± 9	2	5	8
31	−51.584	−72.600	153	2009	2011	3	22	D/-	2 ± 6	1	3	6

[a]("D/-" means direct mount / no antenna change), ("T/A" indicates tripod or tribrach mount and antenna change).

geodetic antennas were implemented. At the semi-permanent stations (22) and (24) Trimble 4700 receivers with Trimble compact geodetic antennas were installed. The duration of occupations at each site were generally from 4 to 10 days of continuous recordings. Early observational campaigns (1996–2001), at sites (14), (18), (10), (12), (15), and (16), were more limited due to power and data-memory capacity. Hence, daily recordings limited to about 10 h each, were acquired. An overview about the sites and their observation scheme is summarized in Table 1.

2.2. Data Analysis

The GPS data were processed with the Bernese GNSS Software version 5.1 [*Dach et al.*, 2007]. Absolute phase-center corrections for transmitter satellite and receiver antennas, which are consistent to IGS-08 reference frame [*Rebischung et al.*, 2012], were applied. The tropospheric delay was modeled with the Vienna mapping function [*Boehm and Schuh*, 2004; *Kouba*, 2008], including 2-hourly zenith delay estimates. Higher-order ionospheric corrections are considered following the approach of *Fritsche et al.* [2005]. Body tide, ocean tidal loading, and atmospheric loading corrections were applied. In order to assure a homogeneous data set for satellite orbits and Earth rotation parameters over the whole observation period, updated products of a new GPS and Global Navigation Satellite System reprocessing [*Fritsche et al.*, 2013] are employed. Those IGS network stations that link our local network to the global terrestrial reference frame (IGS-08) are shown in Figure 1b.

3. Results

3.1. Station Coordinates and Linear Rates

The GPS observations of 31 stations together with data of up to 8 reference stations from the IGS network (Figures 1a and 1b and Table 1) were organized into daily 24 h sessions producing normal equations. Apply-

ing these normal equation combinations, our daily, campaign and final solutions were obtained. Station positions referenced to epoch 2005.00 and linear rates of the coordinates were determined for each site. The uplift rates determined are shown in Table 1. The maximum uplift rate of 41 ± 3 mm/yr was measured at the northwestern rim of Nunatak Viedma at site (16) located in the center of the SPI. Nearby stations, such as (15), (12), (11), (10), and (13) comprise the area of maximum vertical rates with values of 33 mm/yr and more. Further north, the vertical rates slowly decrease, reaching about 20 ± 2 mm/yr in the northern-most site. Also to the west in the fjord area (sites (17), (14), and (9)) the uplift rates decrease from about 20 ± 3 mm/yr down to 4 ± 6 mm/yr. All sites in the southern part of the SPI (sites (19) to (31)) have rates below 20 ± 2–9 mm/yr with diminishing amplitude as the distance to the SPI increases. The smallest rate here is just 2 ± 6 mm/yr (site (31)). Our observed uplift rates are shown in Figures 1d and 2c with the site solutions represented by color-coded disks. The horizontal rates (after subtraction of plate motion) do not allow an unambiguous interpretation of the GIA-only signal, as the overprint of the interplate tectonic deformation makes this impossible (see also discussion in *Dietrich et al.* [2010]).

3.2. Accuracies

To assess the quality of our solutions, we first computed the scatter of the daily coordinate solutions with respect to the campaign mean. These are the so-called daily repeatabilities for the height component and they are on the order of ± 4 mm. However, since the time series of GPS coordinates are not uncorrelated (white noise model), one has to account for correlation of the daily solutions (power noise model). This requires a scaling of the error measure (daily repeatabilities) by a factor of 2–5 [*Zhang et al.*, 1997; *Williams et al.*, 2004]. Here we applied a factor of 3. For the campaign solutions we account for possible larger errors at stations where tripods or tribrachs were used (see Table 1). We allow for an additional error of 10 mm, accounting for a more poorly determined antenna height. Although the absolute antenna phase-center corrections are applied with the IGS standards, we add an additional uncertainty of 10 mm when the antenna type has been changed between campaigns. At GPS sites with direct antenna mount and reoccupations with the same antenna type, errors of this kind are not included in the error budget. Thus, uncertainties of the station heights per campaign are in the order of 3–15 mm. These errors are then propagated in the formal solutions for uplift rates. For the vertical velocities we add another 2 mm/yr uncertainty describing effects coming from the IGS reference stations used to link our network to the global reference frame. These, for example, may be associated with altered station selections due to availability or, as in the case of the M_W 8.8 Maule Earthquake of 27 February 2010, exclusion due to displacements and nonlinear station motion at Concepción after the event. We believe that our stated root-mean-square values for the vertical rates (Table 1), at about 2–9 mm/yr are in fact, quite conservative. It is evident, that the largest error measures have been obtained for the heights of the sites equipped with tripods or tribrachs stations (10), (12), (14), (15), (16), (18), (28), and antenna-type changes between the occupations, stations (9), (13), (17), and (20). However, the large time span between the first and last observation (up to 15 years) for such stations produces absolute height changes approaching 40 cm, thus reducing the overall error level for our uplift rate solutions. A cross check of the error budget is possible at the sites (11)/(12) and (28)/(29). These pairs of sites are only about 150 m apart. Sites (12) and (28) have been observed with tripod occupations, while at sites (11) and (29) the GPS antennas were directly mounted onto the marker. The difference between the uplift rates is only 3 and 2 mm/yr, respectively, essentially confirming our error estimates (see Table 1). The paired observation sites have differing occupation histories, possibly explaining some of the differences in the station solutions. For other tripod/tribrach sites (especially at the center of the SPI) there is reasonable coherence of the uplift pattern between neighboring stations.

4. Interpretation and Intercomparison With Models

4.1. Crustal Response on Present-Day Ice Mass Changes

It has to be kept in mind that the observed uplift rates are the sum of an immediate elastic response of the Earth crust on present-day ice mass changes and the viscous response on ice load changes in the past. *Willis et al.* [2012] estimated the ice mass loss of the SPI for various temporal subintervals spanning 2000–2012. These 12 years are essentially coeval with the majority of the GPS observations. For the regional pattern of ice mass loss rates determined by *Willis et al.* [2012] we have computed the elastic part of uplift (Figure 1c). The rates at the GPS sites are also shown in Table 1. Clearly, the elastic uplift component may exceed 10 mm/yr over continuous spatial sectors of tens of kilometers, and attain local maxima of about 17 mm/yr. The
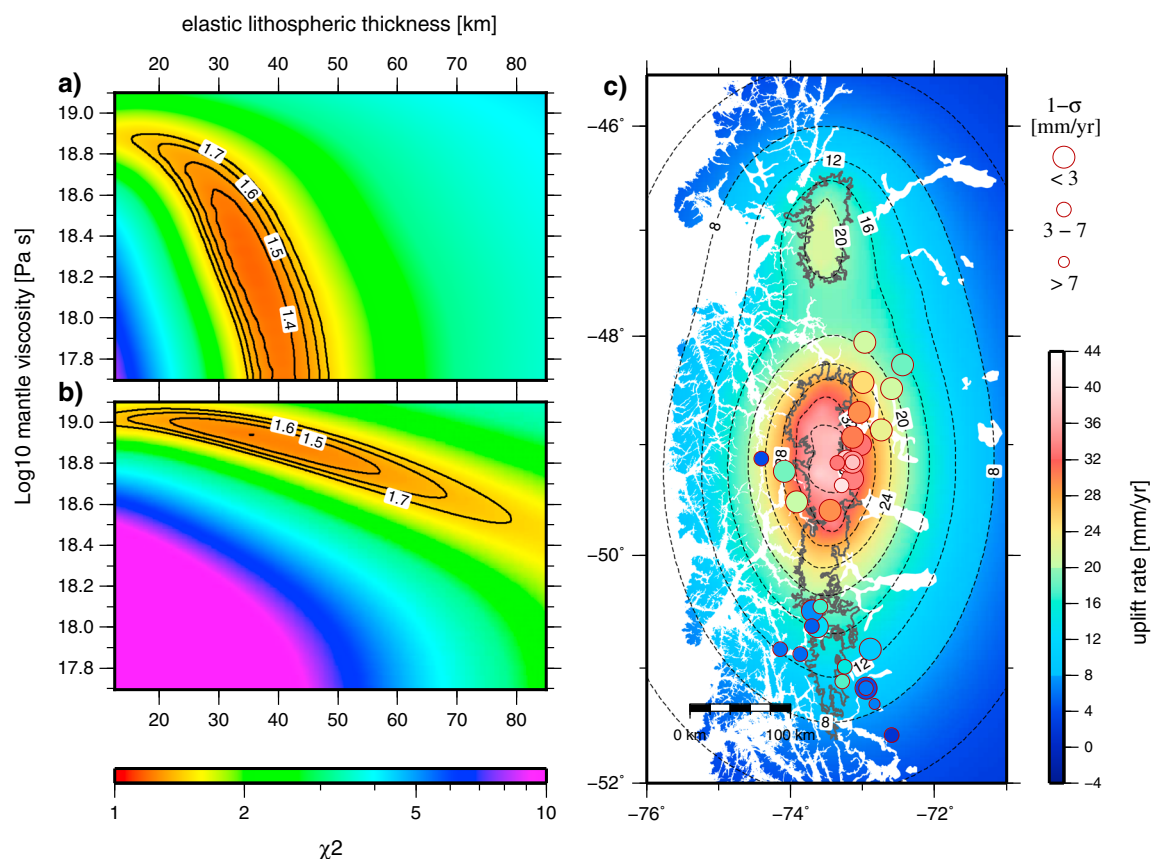
Figure 2. Chi-square test to 31 station uplift data, (a) Model A and (b) Model B. (c) Comparison of regional prediction of vertical crustal motion, refined Model B, with observed uplift rates (color-coded disks).

remaining part of the observed rates may be attributed to a viscoelastic response from earlier load changes, as we test in the next section.

4.2. Comparison With and Refinement of Viscoelastic Models and the Ice Load

The technical details of the solid Earth theory and application to the complex Neoglacial loading and unloading of southernmost South America that is employed has been fully described in *Ivins and James* [1999]. The models assume growth and decay of ice mass prior to the LIA maximum at AD 1630 (also see *Ivins and James* [2004]). We begin by updating a new loading history, the starting model based upon the analysis described in *Dietrich et al.* [2010], as constrained by four station uplift trends and by GRACE Jet Propulsion Laboratory mascon analysis [*Ivins et al.*, 2011]. The load model employed in *Dietrich et al.* [2010] (henceforth, "D10") used a reanalysis of the rates of mass loss determined by *Rignot et al.* [2003]. The ice loss extrapolated into the years 2002–2006 in D10 is −32 Gt/yr for the SPI and −2.5 Gt/yr for Northern Patagonian Icefield (NPI) (as noted in Table 3 of D10). An extrapolation backward in time assumed a complicated method related to Southern Hemispheric surface atmospheric temperature and glacier size as roughly approximated by *Oerlemans* [2005]. The loading-unloading computed in *Ivins et al.* [2011] modified this history: First, after iterating between uplift and GRACE observation, it was determined that the mass loss needed to be lowered to −26 Gt/yr, and the "oldest" segment of the piecewise linear mass loss, 1870–1943, was raised to −11.2 Gt/yr. In the current work, further steps were taken to modify the load. First, we compute a Greens function elastic response due to present-day ice mass change of the SPI (Figure 1c) as determined by *Willis et al.* [2012]. The analysis of both, the height change data and elastic response suggest more ice losses north of 50°S and indicate larger ice loss in the eastern side of the ice fields except north of 49°S. These two features are roughly accounted for. Both the scattered intervals of differencing for time period (2000–2012) and potentially underestimated errors/biases in digital elevation model differencing, motivate our adhering to the patterns, but not necessarily the amplitudes of loss computed in *Willis et al.* [2012] for our purposes of GIA modeling. Secondly, a series of smaller glaciers outside of the SPI and NPI

Table 2. Ice Mass Loss for Models A and B[a]

Model	since LIA (Gt)	1630–1869 (Gt/yr)	1870–1943 (Gt/yr)	1944–1975 (Gt/yr)	1976–1994 (Gt/yr)	1995–2013 (Gt/yr)	Mant. Visc. (Pa s)
Model A	1337	0.0	−11.2	−4.5	−8.6	−10.7	1.6×10^{18}
Model B	1337	−0.009	−6.8	−4.7	−10.5	−25.9	8×10^{18}

[a]Applied ice load history (mass rates) and obtained mantle viscosity η.

(at about 47°15′ S, 73°30′ W), as mapped by *Masiokas et al.* [2009] and *Glasser et al.* [2011], are additionally accounted for. An important third step is to account for the load history (see Table 2). The first model: "A" is characterized by the smallest estimate of present-day SPI loss rates at about −11 Gt/yr determined by TanDEM–X radar height differences between 2000 and 2012 [*Floricioiu et al.*, 2012] with nearly equal loss rates due to climate warming between 1870 and 1943 [*Oerlemans*, 2005]. The second model: "B" assumes an early unloading that is more adherent to the model reconstruction recently considered by *Glasser et al.* [2011] (henceforth, G11) wherein losses between 1870 and 1943 are an order of magnitude smaller than in Model A. For the SPI we allow LIA maximum to be at AD 1630, but with very small −0.009 Gt/yr loss rates until AD 1870. For purpose of comparison both models considered here have a total (SPI+NPI) ice field LIA mass loss of 1337 Gt since AD 1870. Model B has a total (SPI+NPI) loss rate between 1995 and 2013 at −25.9 Gt/yr, rather consistent with the reports of *Ivins et al.* [2011]; *Jacob et al.* [2012], *Willis et al.* [2012], and *Gardner et al.* [2013]. Some features of the G11 model of post-LIA retreat may be implausible for these predicted rates of ice loss amounting to 0.008 mm/yr mean global sea level rise equivalent averaged over time since LIA maximum. The inferred mass loss rates by G11 are at the −2.8 Gt/yr level for the SPI+NPI, until the space-observing period (starting in about 1993–1995) when they jump to −35.9 Gt/yr. Although our Model B is similar to that proposed by G11, it is not designed to mimic precisely the reported values of the latter. In fact, Model B, is more similar to the mass changes during the mid-twentieth century that are inferred by *Aniya et al.* [1997], with a more moderate acceleration of losses during the late twentieth century, and an initial drawdown of mass at the end of LIA maximum that is sensitive to warming climate, but not in any dramatic way. It should be noted that G11 use a comprehensive study of the glacial moraine data and space observations, but our Model B is only more roughly consistent with the G11 than is Model A. What is remarkable in our use of the two end-members is that they may both reconcile the GPS uplift data reported in this paper. Yet they do so with solved-for mantle viscosity, η, that differ by a factor of 5. Using the mean value of χ^2 minima at 1.325 and 1.400 levels for the two models (A and B, respectively), we estimate the lithospheric thickness at 36.5 ±5.3 km (see Figure 2, results for Model B are presented in Figure 2c).

5. Conclusions

The determination of GPS uplift trends using station data taken between 1996 and 2011 provide a unique set of observations that allow us to better understand both post-LIA climate changes and the mechanical structure of the Earth on timescales similar those of postseismic relaxation, but of quite different forcing and internal stress distribution [e.g., *Freed et al.*, 2010]. The GPS network nicely straddles the SPI, thus sampling a sufficiently long wavelength of the deformation field. The data and model appear to deliver tight constraints on the effective elastic lithospheric thickness, at 36.5 ± 5.3 km. It is interesting to note that this value coincides with theoretical and experimental estimates of the elastic thickness of oceanic lithosphere by *Mei et al.* [2010, especially Figure 8, therein]. This coincidence possibly offers some clues as to the thermomechanical state of a tectonic environment that has absorbed an oceanic ridge by recent subduction. Taper methods that combine static gravity and topography to solve for "T$_e$", a longer term estimate of elastic lithospheric thicknesses, are about 30–40 km in *Pérez-Gussinyé et al.* [2009]. Solutions for mantle viscosity are, however, non-unique. If we should place greater faith in a more minimalistic post-LIA ice mass retreat [*Glasser et al.*, 2011], and a large ice loss sustained since about 1995 [*Rignot et al.*, 2003; *Chen et al.*, 2007; *Ivins et al.*, 2011; *Jacob et al.*, 2012; *Gardner et al.*, 2013] (our Model B), then the solved-for mantle viscosity is near 8×10^{18} Pa s. This value is rather consistent with the recent models of post-LIA GIA uplift in Alaska by *Sato et al.* [2011] and *Elliott et al.* [2010]. The alternative ice load model has smaller present-day ice loss rates over the past 18 years, which are nearly equal to those occurring during the first 73 years of collapse from LIA maximum (our Model A scenario). The corresponding mantle viscosity for the latter load history is near 1.6×10^{18} Pa s. We conclude that Model A, while having slightly smaller χ^2 residuals, is less plausible from both the perspective of glaciological inferences and tectonic ana-

logues [cf. *Johnson et al.*, 2013]. While there are relatively few estimates of upper mantle viscosity in 5–12 Ma age slab window mantle environments to compare to, past estimates provide either upper bounds at 5×10^{19} Pa s [*Zandt and Carrigan*, 1993] or, via models of earthquake cycle modulated strain–rate patterns, at a value near 1.2×10^{19} Pa s [*Pollitz and Nyst*, 2005]. Both of the latter estimates are south of the northward migrating Mendocino Triple Junction in northern California, for which there exists high quality seismic imaging of the mantle slab window structure [*Liu et al.*, 2012]. The comparisons to these regions also favor the viscosity solutions of our Model B.

References

Aniya, M., H. Sato, R. Naruse, P. Skvarca, and G. Casassa (1997), Recent glacier variations in the Southern Patagonia Icefield, South America, *Arctic Alpine Res.*, *29*(1), 1–12.

Boehm, J., and H. Schuh (2004), Vienna mapping functions in VLBI analyses, *Geophys. Res. Lett.*, *31*, L01603, doi:10.1029/2003GL018984.

Casassa, G., J. L. Rodríguez, and T. Loriaux (2014), A new glacier inventory for the Southern Patagonia Icefield and areal changes 1986-2000, in *Global Land Ice Measurements From Space (GLIMS), Geophysical Sciences*, edited by J. S. Kargel et al., pp. 810, Springer Praxis Books, New York.

Chen, J., C. Wilson, B. Tapley, D. Blankenship, and E. Ivins (2007), Patagonia icefield melting observed by Gravity Recovery and Climate Experiment (GRACE), *Geophys. Res. Lett.*, *34*, L22501, doi:10.1029/2007GL031871.

Dach, R., U. Hugentobler, P. Fridez, and M. Meindl (Eds.) (2007), *Bernese GPS Software Version 5.0*, Astronomical Institute Univ. of Bern, Switzerland.

Dietrich, R., E. Ivins, G. Casassa, H. Lange, J. Wendt, and M. Fritsche (2010), Rapid crustal uplift in Patagonia due to enhanced ice loss, *Earth Planet. Sci. Lett.*, *289*, 22–29, doi:10.1016/j.epsl.2009.10.021.

Elliott, J. L., C. F. Larsen, J. T. Freymueller, and R. J. Motyka (2010), Tectonic block motion and glacial isostatic adjustment in southeast Alaska and adjacent Canada constrained by GPS measurements, *J. Geophys. Res.*, *115*, B09407, doi:10.1029/2009JB007139.

Floricioiu, D., J. W. Abdel, and H. Rott (2012), Surface elevation changes and velocities on the Southern Patagonia Icefield derived from TerraSAR-X and TanDEM-X, paper presented at ESA CLiC EO Cyosphere ESRIN, Frascati.

Freed, A., T. Herring, and R. Bürgmann (2010), Steady-state laboratory flow laws alone fail to explain postseismic observations, *Earth Planet. Sci. Lett.*, *300*, 1–10, doi:10.1016/j.epsl.2010.10.005.

Fritsche, M., R. Dietrich, C. Knöfel, A. Rülke, S. Vey, M. Rothacher, and P. Steigenberger (2005), Impact of higher-order ionospheric terms on GPS estimates, *Geophys. Res. Lett.*, *32*, L23311, doi:10.1029/2005GL024342.

Fritsche, M., K. Sośnica, C. Rodríguez-Solano, P. Steigenberger, K. Wang, R. Dietrich, R. Dach, U. Hugentobler, and M. Rothacher (2013), *Joint Reprocessing of GPS, GLONASS and SLR*, EGU General Assembly 2013, Vienna, Austria.

Gardner, A., et al. (2013), A reconciled estimate of glacier contributions to sea level rise: 2003 to 2009, *Science*, *340*, 852–857, doi:10.1126/science.1234532.

Glasser, N., S. Harrison, K. Jansson, K. Anderson, and A. Cowley (2011), Global sea-level contribution from the Patagonian Icefields since the Little Ice Age maximum, *Nat. Geosci.*, *4*, 303–307, doi:10.1038/ngeo1122.

Ivins, E., and T. James (1999), Simple models for late Holocene and present-day Patagonian glacier fluctuations and predictions of a geodetically detectable isostatic response, *Geophys. J. Int.*, *138*(3), 601–624.

Ivins, E., and T. James (2004), Bedrock response to Llanquihue Holocene and present-day glaciation in southernmost South America, *Geophys. Res. Lett.*, *31*, L24613, doi:10.1029/2004GL021500.

Ivins, E., M. Watkins, D.-N. Yuan, R. Dietrich, G. Casassa, and A. Rülke (2011), On-land ice loss and glacial isostatic adjustment at the Drake Passage: 2003–2009, *J. Geophys. Res.*, *116*, B02403, doi:10.1029/2010JB007607.

Jacob, T., J. Wahr, W. Pfeffer, and S. Swenson (2012), Recent contributions of glaciers and ice caps to sea level rise, *Nature*, *482*, 514–518, doi:10.1038/nature10847.

Johnson, A. J., C. F. Larsen, N. Murphy, A. A. Arendt, and S. L. Zirnheld (2013), Mass balance in the Glacier Bay area of Alaska, USA, and British Columbia, Canada, 1995–2011, using airborne laser altimetry, *J. Glaciol.*, *59*, 632–648, doi:10.3189/2013JoG12J101.

Klemann, V., E. Ivins, Z. Martinec, and D. Wolf (2007), Models of active glacial isostasy roofing warm subduction: Case of the South Patagonian Ice Field, *J. Geophys. Res.*, *112*, B09405, doi:10.1029/2006JB004818.

Kouba, J. (2008), Implementation and testing of the gridded Vienna Mapping Function 1 (VMF1), *J. Geod.*, *82*, 193–205, doi:10.1007/s00190-007-0170-0.

Larsen, C. F., R. J. Motyka, J. T. Freymueller, K. A. Echelmeyer, and E. R. Ivins (2005), Rapid viscoelastic uplift in southeast Alaska caused by post-little Ice Age glacial retreat, *Earth Planet. Sci. Lett.*, *237*, 548–560, doi:10.1016/j.epsl.2005.06.032.

Liu, K., A. Levander, Y. Zhai, R. W. Porritt, and R. M. Allen (2012), Asthenospheric flow and lithospheric evolution near the Mendocino Triple Junction, *Earth Planet. Sci. Lett.*, *323*, 60–71, doi:10.1016/j.epsl.2012.01.020.

Masiokas, M., A. Rivera, L. Espizua, R. Villalba, S. Delgado, and J. Aravena (2009), Glacier fluctuations in extratropical South America during the past 1000 years, *Palaeogeogr. Palaeoclimatol. Palaeoecol.*, *281*, 242–268, doi:10.1016/j.palaeo.2009.08.006.

McCrory, P. A., D. S. Wilson, and R. G. Stanley (2009), Continuing evolution of the Pacific–Juan de Fuca–North America slab window system –A trench–ridge–transform example from the Pacific Rim, *Tectonophysics*, *464*, 30–42, doi:10.1016/j.tecto.2008.01.018.

Mei, S., A. Suzuki, D. Kohlstedt, N. Dixon, and W. Durham (2010), Experimental constraints on the strength of the lithospheric mantle, *J. Geophys. Res.*, *115*, B08204, doi:10.1029/2009JB006873.

Oerlemans, J. (2005), Extracting a climate signal from 169 glacier records, *Science*, *308*, 675–677, doi:10.1126/science.1107046.

Pérez-Gussinyé, M., C. J. Swain, J. F. Kirby, and A. R. Lowry (2009), Spatial variations of the effective elastic thickness, T_e, using multitaper spectral estimation and wavelet methods: Examples from synthetic data and application to South America, *Geochem. Geophys. Geosyst.*, *10*, Q04005, doi:10.1029/2008GC002229.

Pollitz, F. F., and M. Nyst (2005), A physical model for strain accumulation in the San Francisco Bay Region, *Geophys. J. Int.*, *160*, 302–317, doi:10.1111/j.1365-246X.2005.02433.x.

Rebischung, P., J. Griffiths, J. Ray, R. Schmid, X. Collilieux, and B. Garayt (2012), IGS08: The IGS realization of ITRF2008, *GPS Solut.*, *16*, 483–494, doi:10.1007/s10291-011-0248-2.

Rignot, E., A. Rivera, and G. Casassa (2003), Contribution of the Patagonia Icefields of South America to sea level rise, *Science*, *302*, 434–437, doi:10.1126/science.1087393.

Sato, T., C. Larsen, S. Miura, Y. Ohta, H. Fujimoto, W. Sun, R. Motyka, and J. Freymueller (2011), Reevaluation of the viscoelastic and elastic responses to the past and present-day ice changes in Southeast Alaska, *Tectonophysics*, *511*, 79–88, doi:10.1016/j.tecto.2010.05.009.

Thatcher, W., and F. F. Pollitz (2008), Temporal evolution of continental lithospheric strength in actively deforming regions, *GSA Today*, *18*, 4–11, doi:10.1130/GSAT01804-5A.1.

Williams, S., Y. Bock, P. Fang, P. Jamason, R. Nikolaidis, L. Prawirodirdjo, M. Miller, and D. Johnson (2004), Error analysis of continuous GPS position time series, *J. Geophys. Res.*, *109*, B03412, doi:10.1029/2003JB002741.

Willis, M., A. Melkonian, M. Pritchard, and A. Rivera (2012), Ice loss from the Southern Patagonian Ice Field, South America, between 2000 and 2012, *Geophys. Res. Lett.*, *39*, L17501, doi:10.1029/2012GL053136.

Zandt, G., and C. R. Carrigan (1993), Small-scale convective instability and upper mantle viscosity under California, *Science*, *261*, 460–463, doi:10.1126/science.261.5120.460.

Zhang, J., Y. Bock, H. Johnson, P. Fang, S. Williams, J. Genrich, S. Wdowinski, and J. Behr (1997), Southern California Permanent GPS Geodetic Array: Error analysis of daily position estimates and site velocities, *J. Geophys. Res.*, *102*(B8), 18,035–18,055, doi:10.1029/97JB01380.